Made available through Montana State University's ScholarWorks

Observation and Modeling of Shear Evolution of Post-reconnection Flare Loops

Drake Osaben; Jiong Qiu; Dana W. Longcope

Accessibility Disclaimer:

For a more accessible version of this document, please submit an accessibility request form through the Montana State University Library website.

The Astrophysical Journal, 995:142 (12pp), 2025 December 20 https://doi.org/10.3847/1538-4357/ae1a86
© 2025. The Author(s). Published by the American Astronomical Society.
OPEN ACCESS

Observation and Modeling of Shear Evolution of Post-reconnection Flare Loops

Drake Osaben, Jiong Qiu, and Dana W. Longcope
Department of Physics, Montana State University, Bozeman, MT 59715, USA
Received 2025 July 31; revised 2025 October 16; accepted 2025 October 30; published 2025 December 11

Abstract

A solar flare releases magnetic energy by reconnecting field lines across a current sheet, thereby allowing their relaxation to a lower-energy state. The maximum possible energy is released if all field lines relax to a current-free (potential) state. The progress of a flare's reconnection is often measured as the angle-complement between the observed post-reconnection flare loops and the polarity inversion line of the photospheric magnetic field: shear angle. Many observations have shown strong-to-weak shear evolution over the course of a flare. A field line's shear angle is, however, an imperfect measure of its relaxation. We develop a new technique for observationally inferring the 3D structure of post-reconnection field lines, including their local twist, , which will vanish for potential fields. Our method fits loops in extreme-ultraviolet (EUV) images to extrapolations subject to constraints such as matching the feet of model field lines to observed flare ribbons. We apply the new method to an eruptive two-ribbon flare (SOL2014-12-18T22), which exhibits strong-to-weak shear-angle evolution. We find that, as the flare progresses, decreases in post reconnection loops anchored to newly brightened ribbons. Our study demonstrates that post-reconnection magnetic field is neither potential nor linear force-free. The method quantifies, for the first time, the time-history of a flare's energetic relaxation. It also quantifies the increasing height of the subsequently reconnected field, and the time delay between reconnection forming a flare loop and its appearance in EUV passbands. These results promise to enable improvements in both magnetic modeling and hydrodynamic modeling of flares.

Unified Astronomy Thesaurus concepts: Solar magnetic reconnection (1504); Solar flares (1496); Solar extreme ultraviolet emission (1493); Solar magnetic fields (1503)

1. Introduction

A solar flare releases free magnetic energy by magnetic reconnection that relaxes the magnetic field to a lower-energy state. The configuration of a particular type of flares, eruptive two-ribbon flares, has been depicted by the standard model, well known as the Carmichael–Sturrock–Hirayama–Kopp–Pneuman (CSHKP) model (H. Carmichael 1964; P. A. Sturrock 1966; T. Hirayama 1974; R. A. Kopp & G. W. Pneuman 1976). The model explains a number of key observational signatures: magnetic reconnection occurs in the corona between a set of antiparallel magnetic field lines across a vertical current sheet and forms an arcade of flare loops in the corona with their feet anchored in a pair of flare ribbons in the chromosphere on the two sides of the polarity inversion line (PIL) separating positive and negative magnetic flux. Most of the reconnection released energy rapidly deposits at the feet of the flare loops, producing bright flare ribbons. The impulsive energy deposition in the chromosphere drives mass upflows (chromospheric evaporation; E. Antonucci et al. 1982; G. H. Fisher 1987) into the coronal loops, which then become prominently visible in the soft X-ray and then extreme-ultraviolet (EUV) light as they cool from a few tens to a few million kelvin. The pair of flare ribbons in the chromosphere is observed in visible, ultraviolet (UV), and, every now and then, hard X-ray (HXR) emissions. Observations often show that the two flare ribbons move away from the PIL during the flare (Z. Svestka 1980; T. Kitahara & H. Kurokawa 1990; T. Sakao 1994; L. Fletcher & H. Hudson 2001; H. Isobe et al. 2002; J. Qiu et al. 2002, 2017; A. Asai et al. 2004; M. Temmer et al. 2007; C. Liu & H. Wang 2009; Y.-H. Yang et al. 2011; M. D. Kazachenko et al. 2017; J. Hinterreiter et al. 2018). The apparent ribbon motion is interpreted as a signature of progressive magnetic reconnection proceeding continuously and forming taller, and presumably longer, loops with their conjugate feet at a progressively larger distance from each other.

Despite its success in capturing the global signatures of flare evolution, the standard model cannot account for many other properties of flare reconnection. Flares tend to occur in sheared magnetic fields (C. J. Schrijver et al. 2008; M. G. Bobra & S. Couvidat 2015; S. Patsourakos et al. 2020), where reconnection must take place between a pair of field lines that are not antiparallel (i.e., component reconnection). Therefore, post-reconnection field lines will carry a nonvanishing component along the direction of the current, which is also the direction of the PIL in a 2D or 2.5D[1] configuration. Such a feature has been characterized observationally by the shear angle θ of post-reconnection flare loops (PRFLs), defined as the complement of the angle between a PRFL projected on the solar surface and the PIL of the vertical component of the photospheric magnetic field. Observations of many eruptive flares have shown that earlier formed flare loops, when viewed top-down in disk observations, appear to have a larger shear angle, than later-formed loops. This is known as the "strong-to-weak" shear evolution of PRFLs (M. J. Aschwanden & D. Alexander 2001).

The apparent shear angle of PRFLs has been measured in a number of studies over two decades. Before the Solar Dynamics Observatory (SDO; W. D. Pesnell et al. 2012) was launched, the apparent shear angle $\theta_{\rm ft}$ was estimated by measuring the angle between the PIL of the line-of-sight component of the photospheric magnetic field, approximated as a

Original content from this work may be used under the terms of the Creative Commons Attribution 4.0 licence. Any further distribution of this work must maintain attribution to the author(s) and the title of the work, journal citation and DOI.

[1] 2.5D refers to the configuration with a symmetry direction over which quantities do not vary but along which vectors may have nonvanishing components.

straight line, and another straight line connecting a pair of flare kernels or centroids of flare ribbons observed in optical (H. Ji et al. 2006), UV (Y. N. Su et al. 2006; Y. Su et al. 2007), or HXR (T. Sakao 1994; S. A. Bogachev et al. 2005; P. C. Grigis & A. O. Benz 2005; W. Liu et al. 2009; Y.-H. Yang et al. 2009; A. R. Inglis & H. R. Gilbert 2013; I. V. Zimovets et al. 2020) emissions. These methods primarily assume the magnetic connectivity between the most prominent pair of flare kernels or centroids of flare ribbons. The strong-to-weak shear evolution was often, though not always, associated with the parallel-to-perpendicular apparent motion of flare ribbons or kernels with respect to the PIL, which is often curved rather than straight. J. Qiu (2009), J. Qiu et al. (2010, 2017), and J. Qiu & J. Cheng (2022) therefore defined a shear index $\mathcal{S} \equiv \Delta\langle l_{\|}\rangle / \Sigma\langle l_{\perp}\rangle$, where $\langle l_{\|}$ is the distance of the centroid of flare ribbon fronts along the curved PIL, $\langle l_{\perp}$ is the mean distance of the centroid perpendicular to the PIL, and Δ and Σ refer to the difference and sum, respectively, of the measurements for ribbons in the positive and negative magnetic fields. The shear index is another proxy of the mean shear of the post-reconnection flare arcade with respect to the curved PIL, and measurements in several two-ribbon flares reported in these papers also confirmed the strong-to-weak shear evolution with $\mathcal{S}$ varying from up to 5 at the start of the flare to below 2 or 1 when the flare HXR emission at $>$20 keV peaks.

Observational studies in recent years have taken advantage of PRFLs directly observed by SDO's Atmosphere Imaging Assembly (AIA; J. R. Lemen et al. 2012). T. Li et al. (2019) measured the shear $\theta_{\rm lp}$ between several PRFLs with the PIL of the line-of-sight photospheric magnetic field in about 20 flares. J. Qiu et al. (2017) measured the shear in a slightly different way, where $\theta_{\rm lp}$ is derived from the angle of a set of observed loops with the PIL of the extrapolated potential magnetic field at an assumed height of the loops. Most recently, J. Qiu et al. (2023) identified up to 3000 PRFLs from AIA observation in two EUV passbands characterized by plasmas of 1 MK. The general trend of the $\theta_{\rm lp}$ also exhibits the strong-to-weak shear evolution, and is consistent with shear index evolution derived from the ribbons.

The strong-to-weak shear evolution, and the apparent parallel motion of flare kernels or ribbons, are clear observational signatures of 3D magnetic reconnection (G. Aulanier et al. 2012; M. Janvier et al. 2013). On the other hand, shear angle measurements have been constrained to information in the image plane, and the shear angle $\theta_{\rm ft}$, $\theta_{\rm lp}$, and the shear index $\mathcal{S}$, are, at best, *proxies* of some 3D reconnection properties. Furthermore, the measurements are subject to ambiguities introduced by the often complex shape of the photospheric PIL (e.g., A. R. Inglis & H. R. Gilbert 2013). It is, therefore, difficult to interpret the exact physical meaning of the observed shear evolution. Some idealized numerical models of flare reconnection can reproduce the observed strong-to-weak shear evolution (J. T. Dahlin et al. 2022), with the setup of a *pre-reconnection* magnetic field that has a smooth distribution in the photosphere, a straight PIL, and more sheared field lines near the PIL. These studies imply that the observed strong-to-weak shear evolution of PRFLs may be reminiscent of the *pre-reconnection* field configuration. The observational measurements of shear evolution, however, must be associated with *post-reconnection* configurations. It remains to be understood how reconnection relaxes the pre-reconnection field to generate the observed post-reconnection signatures. The 3D magnetic field in active regions, both before and after flare reconnection, is more complex than idealized MHD models (e.g., X. Sun et al. 2012). The post-reconnection field describing the observed PRFLs has not been modeled, yet it is crucial for understanding relaxation of magnetic field by flare reconnection.

In this paper, we present a novel experiment that constructs the 3D magnetic field of PRFLs of an M6.9 eruptive two-ribbon flare to understand the physical nature of the strong-to-weak shear evolution. The model field is an optimized fit to the observed PRFLs, with the constraint that field lines must be anchored to observed flare ribbons. In the following sections, we present an overview of the flare and 3000 PRFLs identified from EUV images (Section 2). We describe in Section 3 the data-constrained method, the Optimized Ribbon-Constrained Constant- (ORCCA) fitting method, to model these 3000 PRFLs. Our results show that PRFLs that formed earlier deviate more from the potential field than those that later formed PRFLs (Section 4). The physical implications of these results are discussed in Section 5.

2. Overview of Observations

The SOL2014-12-18 M6.9 flare was accompanied by a coronal mass ejection. Comprehensive descriptions of the flare observed by multiple telescopes were provided in N. C. Joshi et al. (2017) and J. Qiu et al. (2023), and data-driven MHD simulations of the eruption were conducted by A. Prasad et al. (2023). For this event, a large number of PRFLs are visible in the EUV images in the 304 and 171 Å passbands of AIA throughout the flare evolution. EUV images in other EUV bands are largely saturated and are therefore not analyzed in this study.

The PRFLs can be identified using the Oriented Coronal CUrved Loop Tracing algorithm (OCCULT; M. J. Aschwanden 2010). The code applies a high-pass filter to identify bright pixels against the background, and traces neighboring bright pixels that form an arc, which is considered to be a loop, or part of a loop. J. Qiu et al. (2023) applied the OCCULT code to EUV observations of this flare. In the 304 Å passband, 1980 loops, or parts of loops, were identified between 21:55 and 22:47 UT using 201 images of 12 s cadence. Images in the 171 Å passband are saturated in the early phase of the flare, so the analysis was applied to 98 images (of 24 s cadence) between 22:04 and 22:46 UT, yielding 933 loops. Figure 1 shows the PRFLs observed in the 304 Å images (top panels), and also the PRFLs identified from these images (bottom panels), superimposed on a magnetogram of the photospheric radial magnetic field obtained by the Helioseismic and Magnetic Imager (HMI; J. Schou et al. 2012). Note that a single PRFL may be identified in multiple frames in an EUV passband since loop emission typically persists for a few minutes in the passband (M. J. Aschwanden & D. Alexander 2001; J. Qiu & D. W. Longcope 2016). Also note that a single PRFL in one EUV image may appear as several disconnected parts or sections and, therefore, is identified as several "loops." As a result, the OCCULT code has identified more than 1000 loop-like structures in one passband during the flare evolution. For simplicity, we refer to all of these structures as "loops" in the following text. J. Qiu et al. (2023) analyzed and modeled the evolution of these loops identified in the 304 and 171 Å passbands, and found that loops identified in these two passbands form at nearly the same temperature, $\leqslant$1 MK.

Figure 1(f) also shows the evolution of flare ribbon brightening observed in the AIA 1600 Å images. The color indicates

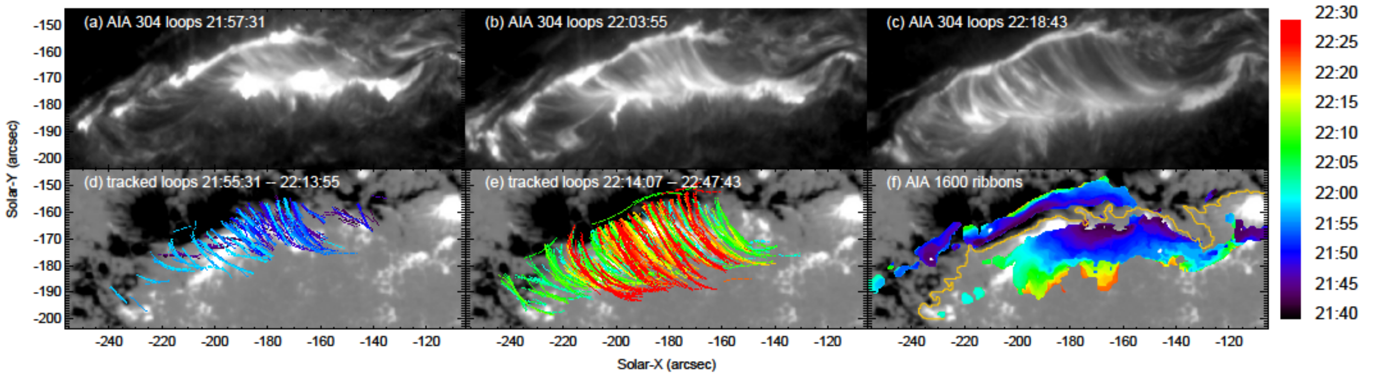

Figure 1. Top panels: post-reconnection flare loops observed in the EUV 304 Å images by AIA at different times. Bottom panels: (d)–(e) PRFLs identified from the AIA 304 Å images using the OCCULT code, superimposed on a magnetogram of the photospheric radial magnetic field obtained by the Helioseismic Magnetic Imager (HMI) at 21:00 UT. The colors indicate the times when the loops were observed in the AIA 304 Å images minus 15 minutes. (f) Evolution of flare ribbons observed in the AIA 1600 Å passband, with the colors of the contour indicating the time the ribbon pixels are brightened, as denoted in the color bar in the right. The orange curve outlines the PIL of the photospheric radial magnetic field (grayscale). All images in this figure have been rotated to 21:00 UT, and the helioprojective coordinates in the figures reflect this reference time.

the onset time of the ribbon brightening, defined as when a ribbon pixel becomes 6 times brighter than the pre-flare quiescent Sun and continues to be bright for more than 4 minutes (J. Qiu et al. 2023; J. Qiu & R. Fleming 2025). We consider that this is approximately the time when reconnection occurs in the corona forming a PRFL anchored at the UV-brightened pixel. Figure 1(f) therefore shows the evolution of flare reconnection forming the PRFL arcade. Seen from the figure, the identified PRFLs are apparently anchored at the two ribbons in magnetic fields of opposite signs. On the other hand, PRFLs become visible more than 10 minutes after the ribbon brightening, reflecting the timescales of plasma heating and then cooling to 1 MK to be observed in these passbands.

Seen from the figure, earlier formed PRFLs (violet and blue) appear to be more inclined toward the PIL of the photospheric magnetogram than later-formed PRFLs (green, orange, and red), suggesting the strong-to-weak shear evolution as reported in many previous studies. For this flare, the strong-to-weak shear evolution was inferred from the evolution of flare ribbons (J. Qiu & J. Cheng 2022), and was then confirmed with $\theta_{\rm lp}$ measured with 3000 PRFLs observed in AIA 304 and 171 passbands characterizing plasma emission at 1 MK (J. Qiu et al. 2023). In this paper, we will model the 3D magnetic structure of these loops to better understand the nature of the shear evolution.

3. Modeling the Magnetic Field of Post-reconnection Flare Loops

In solar flares, magnetic reconnection forms PRFLs, which then relax on Alfvénic timescales, typically of a few seconds, under magnetic Lorentz force. Plasmas inside PRFLs are heated to more than 10 MK and then cool down to 1 MK in 10^{0-1} minutes. Therefore, we consider PRFLs observed in the EUV passbands characteristics of plasma temperature 1 MK to be nearly force free, satisfying $\times \boldsymbol{B} = \boldsymbol{B}$, where is the force-free parameter. Conventionally, the 3D magnetic field is constructed using an extrapolation method that solves the force-free equation and Maxwell equations, subject to the boundary condition provided by the photospheric magnetograms (see review in T. Wiegelmann & T. Sakurai 2021). In the case of a linear force-free field (LFFF), the force-free parameter is a constant, and the normal component of the magnetic field in the photosphere is used as the boundary condition. For a nonlinear force-free field (NLFFF) with varying , all three components of the vector magnetic field measured in the photosphere are used as the boundary condition.

In this study, we find that the observed PRFLs cannot be well described by a single value of , which means that the field associated with PRFLs is not a constant- force-free field (i.e., LFFF). Our intent, however, is to characterize PRFLs immediately following their relaxation in the midst of a flare. The ongoing flare compromises the vector field measurements, making their use in a full NLFFF extrapolation problematic. Moreover, the overall field is rapidly evolving during the flare, and is not an equilibrium. While each PRFL is assumed to be fully relaxed, and thus in equilibrium, the field nearby is undergoing continuous reconnection and retraction, and will not be in equilibrium. Therefore, we develop a different approach to approximate the 3D force-free equilibrium, with spatially varying , using several kinds of observations, rather than the magnetograms alone, to constrain the model. We hereafter refer to this method as Optimized Ribbon-Constrained Constant- fitting (ORCCA fitting).

ORCCA fits each PRFL, found from an EUV image, to a field line from a particular LFFF, with its prescribed value of . The fitting yields different values of for each field line, so the overall field is not itself a force-free equilibrium. A. Malanushenko et al. (2009) developed and applied a similar method and verified that the collection of field lines, with varying , can approximate a genuine NLFFF with reasonable accuracy. In the present work, we further require model field lines to be anchored in flare ribbons, which are footpoints of PRFLs, observed in the UV 1600 Å by AIA. In this way, ORCCA takes advantage of the information available from both coronal and chromosphere images and photospheric magnetogram.

3.1. The ORCCA Fitting Method

We extrapolate the LFFFs from HMI's cylindrical equal-area map (M. G. Bobra et al. 2014) of the radial component of the magnetic field prior to the flare. The extrapolation is performed in tangent plane coordinates, where the (x, y) plane is tangent to the solar surface, and z is the height above that

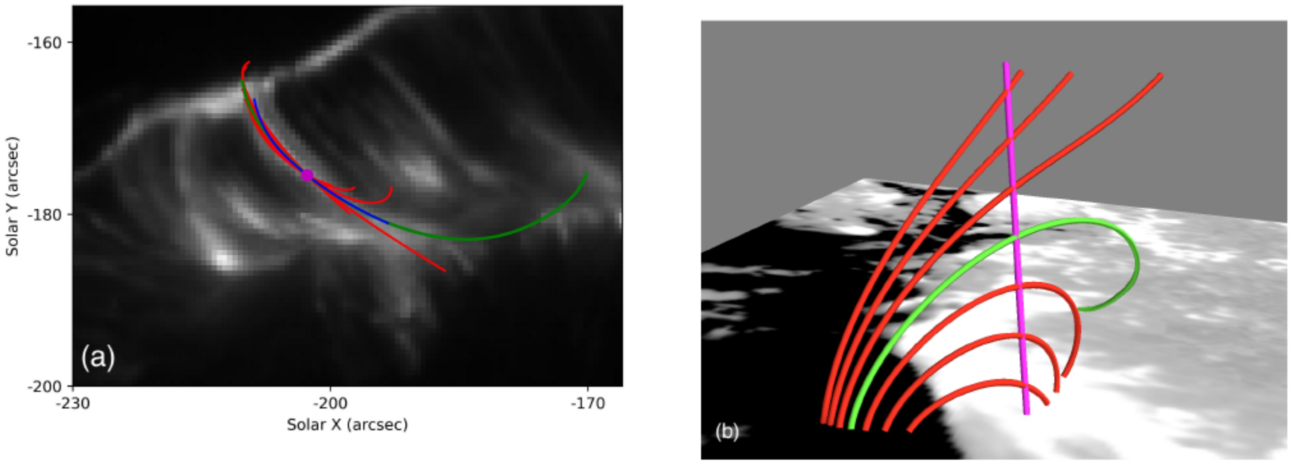

Figure 2. (a) A sample of field lines traced at various heights for a given , overlaid on top of an AIA 304 Å image in which the (blue) observed loop is identified. (b): A side view of the same sample of field lines traced with a CEA magnetogram placed at the surface $z = 0$, saturated at 300 G. In both panels, the magenta color indicates the observed loop's center pixel, red curves show the sample of model field lines traced at various heights, and the green curve shows the modeled loop that is the best fit to observation.

plane. Radial field measurements from HMI are mapped onto the tangent plane (i.e., $z = 0$ surface) and used as a lower boundary to extrapolate an LFFF. Extrapolations are done for each of 50 different values ranging uniformly over $0\,\mathrm{Mm}^{-1}$ $0.2\,\mathrm{Mm}^{-1}$. The range of values used in this experiment is chosen by visually comparing the extrapolated field lines with subsets of PRFLs observed during various stages of the flare.

We use each of the 50 fields to generate magnetic field lines in search of a best fit to a particular PRFL. The pixel at the center of the observed PRFL defines a line of sight, which is mapped onto the tangent plane space, as illustrated by the magenta line in Figure 2(b). The center pixel of an observed loop is typically a few pixels away from the PIL, because an observed loop is only part of the full loop, and the PIL is closer to the northern ribbon due to asymmetric magnetic field distribution (see Figure 1(f)). For a given value of , a single field line is traced in both directions from a point H along this line. A set of field lines is traced from 40 different values of H ranging uniformly over $0 < H$ 20 Mm; several are illustrated by the red and green lines in Figure 2(b). These are then mapped back to the plane-of-the sky, as shown in Figure 2(a), where they may be successively compared to the observed PRFL, shown as a blue curve in this figure.

Tracing field lines from 40 different heights, H, for each of 50 different values, results in 2000 projections that must be compared to the single PRFL. We deem the best fit to be that field line which minimizes an error metric with its PRFL; we present the details of the error metric below. A. Malanushenko et al. (2009) followed the same approach, but found that the global minimum over the full (, H) space was not always the most physically plausible field line. They were fitting loops in quiescent active regions, and considered the full set of traced field lines. Considering PRFLs in a flare, as we do, provides several physical constraints by which many of the field lines may be discarded. Of those that remain, we find that the one minimizing the error metric is the most plausible one and, therefore, deem it the best fit. The absence of such physical constraints when considering quiescent active regions forced A. Malanushenko et al. (2009) to define a particular local minimum as the best fit.

Of the 2000 field lines modeling a particular PRFL, we find that most do not satisfy basic properties of a flare loop and, therefore, can be discarded. First, we end the tracing if the field line crosses the upper boundary at $z = 20$ Mm. The maximum separation of the two flare ribbons is about 20 Mm (Figure 1(f)), and we assume that no valid PRFL would exceed that height. Next, we require that a projected field line be longer, in the plane-of-the sky, than the observed loop in order to be valid. Since coronal loops are only partially visible in a particular EUV image (see Figure 2(a)), they are often shorter but never longer than the field line they follow. Finally, we invoke the assumption that flare ribbons observed in AIA UV 1600 Å constitute the feet of the PRFLs. We therefore require a valid field line to have both feet somewhere in the chromospheric flare ribbons. Note that there are uncertainties in identifying flare ribbon pixels; in particular, weakly brightened pixels might be missed (see discussions in J. Qiu & R. Fleming 2025). Furthermore, the width of observed loops is typically a few AIA pixels. To take into account these factors, we smooth the flare ribbon mask (Figure 1(f)) with a 4 x 4 pixel boxing car, and require valid field lines to land inside the smoothed ribbon mask.

These three criteria eliminate a significant fraction of the 2000 field lines from further consideration. For a small number of loops, all 2000 field lines are eliminated, or there is not a valid fit to the loop. For example, a curvilinear structure lying on the northern ribbon in Figure 1(e) (in green) is indeed a section of the ribbon, or a false loop. These few false loops cannot pass the three criteria and are therefore eliminated from the sample. The remaining field lines fitting a loop provide a sparse sampling of the (, H) parameter space, from which the overall shape of the error function cannot be inferred. Therefore, out of the remaining field lines, we take the one minimizing the error metric to be the best fit, as described in the following text.

3.2. Error Metric

We use an error metric, σ, to quantify the degree to which a magnetic field line, projected onto the plane-of-the-sky, accurately represents an observed PRFL. Our error metric measures the average plane-of-the-sky separation between the

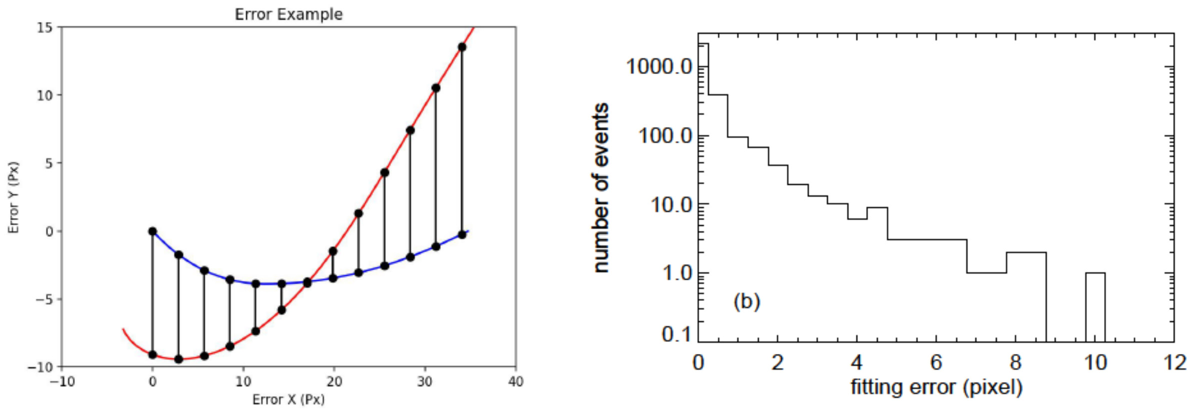

Figure 3. (a) An example demonstrating the error metric between an observed loop (blue) and modeled field line (red). The separation $\Delta Y(X)$ is shown by vertical black lines. (b) Histogram of the fitting error σ for 2807 loops.

field line and its target loop (also see H. P. Warren et al. 2018), so the minimum value provides the best approximation.

We measure the separation as the distance between the two curves, along the direction (Y) perpendicular to the line connecting the ends of the observed PRFL. This line is the X-axis in what we hereafter call "error space," and the loop's ends are located at (0, 0) and ($X_{\max}$, 0), as illustrated by the blue curve in Figure 3. Both curves are rotated into error space and fit with splines, as illustrated by the two curves in Figure 3(a). The separation distance, $\Delta Y(X)$, is computed at regularly spaced values of X covering the full range of the PRFL: $0 \leqslant X \leqslant X_{\max}$. Because we have eliminated field lines shorter than the PRFL, the former will always extend beyond the latter in error space (compare red and blue curves in Figure 3(a)). The error metric, σ, is defined as the average unsigned distance between the curves

$$\sigma = \frac{1}{X_{\max}} \int_0^{X_{\max}} |\Delta Y(X)|\, dX, \tag{1}$$

approximated by the rectangle rule.

Of all valid field lines for a given PRFL, we designate the best fit as that field line with the minimum value of $\sigma(\ , H)$. Because we discarded most of the 2000 possible field lines, the (, H) parameter space is sparsely sampled and cannot be searched using an algorithm assuming a smooth function. On the other hand, there are few enough points that the minimum can be found through a full search. In practice, we minimize over H for each value of   and then find the minimum of these minima.

ORCCA fitting associates with every observed PRFL a 3D field line along with a value of twist, . It only fails in cases (about 4% in our study) where none of the 2000 possible field lines satisfy the criteria. Figure 3(b) shows the distribution of the minimum σ for the remaining 2807 loops (96%), indicating that the mean separation between observed and model field line is well within 2–3 AIA pixels, which is the minimal observed loop width (M. J. Aschwanden & H. Peter 2017). The very few loops with $\sigma > 3$ pixels are discarded.

Of the remaining 2728 (94%) loops that are successfully fit, each has a 3D geometry and a value of . As each one is generated from a different LFFF, they cannot be combined into an equilibrium field. Nevertheless, we expect each field line to be a reasonable approximation, in three dimensions, of the actual PRFL after it has relaxed following reconnection (A. Malanushenko et al. 2009). In more than one-half of the successful cases, the length of the projected best-fit field line is between 1 and 3 times the length of the observed loop. Since an observed loop is only part of a full loop, we subsequently develop a method to identify different parts of the same loop in Section 3.3.

3.3. Identification of Unique PRFLs

Among the 2728 loops successfully fit by ORCCA, there are undoubtedly instances of the same physical loop identified at multiple times. AIA observations at 12 s cadence are able to capture a single loop multiple times as its plasma cools through an EUV passband—typically on a timescale of minutes. Sometimes, a loop may appear broken into multiple segments in a single image, which are recognized by OCCULT as several loops. Each observation of a given PRFL can therefore be fit multiple times by different modeled field lines. Identifying and consolidating cases where a single field line has been fit multiple times provides a better representation of the reconnection process. It also offers the opportunity of estimating the uncertainty in our new methodology.

We attempt to identify and consolidate repeat observations of the same PRFL over a 4 minute window. The time window is based on the expected time for a PRFL to cool through a particular passband (e.g., M. J. Aschwanden & D. Alexander 2001; J. Qiu & D. W. Longcope 2016). An example of all of the observed loops in one time window is plotted in red in Figure 4(a), superimposed on an AIA 304 Å image. It appears possible that some of these are repeat observations of the same loop, or partial sections of that loop.

The model field line of the longest observed loop within the 4 minute window is taken as a reference, and compared to all others within the window to find any repeats. It is compared using error metric, σ_m, defined in Equation (1), but computed between the reference field line and all other observed loops. Each loop with $\sigma_m < \sigma_{\rm thr}$, is taken to be a repeat observation of the reference. After removing from consideration the reference loop, and all repeat observations of it (if there are any), we repeat this procedure using the model field line of the longest of the *remaining* observed loops in that time window as the new reference loop. This is iterated until no loops remain in the time window.

We have arrived at the optimal threshold, $\sigma_{\rm thr} = 0.5$ pixel, through experimentation. We find this to match various loop

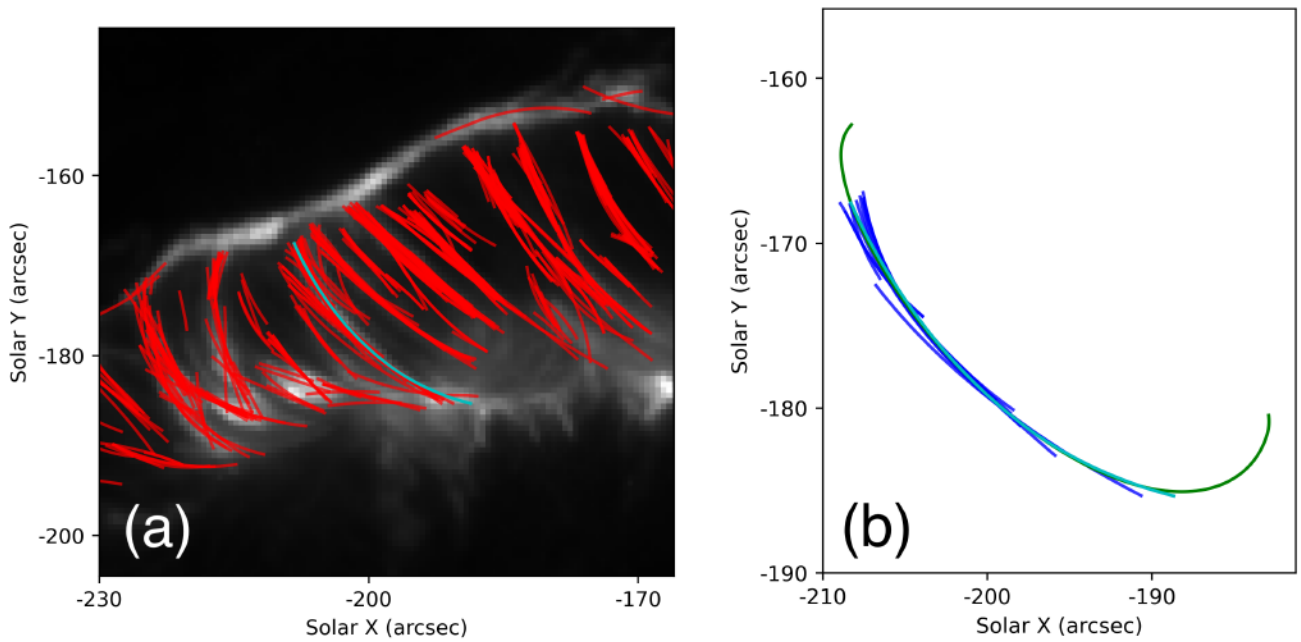

Figure 4. (a) An example of several tens of observed loops in both AIA 304 and 171 Å passbands identified with the OCCULT code (red) within a time window of 4 minutes, superimposed on an AIA 304 Å image. The loop in cyan is one of the reference loops within this time window. (b) A zoomed-in view of the consolidation, showing 12 observed loops (blue) that match a model loop (green) of the longest observed loop, or reference loop (cyan), with σ $\sigma_{\rm thr}$.

sections while avoiding the previously formed, underlying PRFLs. This is a stringent condition considering the average observational width of the loops is >1 AIA pixel (M. J. Aschwanden & H. Peter 2017). With this choice of $\sigma_{\rm thr}$, we reduce the number of PRFLs from 2728 to 920 unique loops. In those cases where the reference field line fits its own loop with $\sigma < 3$ pixel but $\sigma > \sigma_{\rm thr}$, a second match, i.e., repeat, is unlikely. There are almost no repeats in such cases.

Figure 4(b) shows an example of this procedure at work. Among all of the observed loops (red) in the time window, 12 of them (blue) are found to match the field line (green) of the longest observed loop (cyan), with $\sigma_m < \sigma_{\rm thr}$. We take these to be 12 repeat observations of the same loop: reference loop, and hereafter consolidate them into a single field line.

Figure 5(a) characterizes the consolidation process through a histogram of the number N of repeat loops, including the reference itself (i.e., $N \geqslant 1$). Among the 920 loops, 481 of them, or about one-half, have been observed only once ($N = 1$). Each of the other 439 loops appears more than once, as determined by the above algorithm. The histogram falls off geometrically as $(0.67)^N$, which could occur if each successive image had a 67% chance of satisfying the matching criterion. The consolidation of 2728 loops into 920 groups gives an average group size of $\langle N$ $\simeq 3$, matching the mean of the normalized geometric series.

For each of the 439 loops with repeat observations ($N > 1$), the fitting provides multiple measurements of the same quantity. We adopt the value from the reference loop for the consolidated loop, and use the other values to estimate measurement uncertainty. For example, the standard deviation in , denoted as , provides an estimate of measurement uncertainty in . Figure 5(b) is a histogram of the 439 loops over – space. It shows that $< 0.02\ {\rm Mm}^{-1}$ for more than 60% of the loops and $< 0.04\ {\rm Mm}^{-1}$ for more than 90% of the loops. The standard deviation is not strongly correlated with itself.

Finally, Figure 6 shows the field lines of all unique loops, consolidated from nearly 3000 observed loops, viewed from the top (a), and from the side (b). Here, the colors indicate the values from the ORCCA fit. It is shown that loops anchored in the photosphere closer to the PIL tend to have larger values. These properties will be examined in detail in the next section.

The ORCCA method provides this 3D information for each field line. It does not necessarily produce a self-consistent 3D field over the entire volume. As a consequence, some field lines will cross one another, even though this cannot occur in a genuine, force-free field. This appears to affect a small number of field lines shown in Figure 6.

4. Properties and Evolution of PRFLs

We have obtained the 3D quasi-force-free magnetic field describing the PRFLs, with which we characterize the physical nature of flare evolution, including the strong-to-weak shear evolution. Figure 7 shows properties of PRFLs during the entire course of the flare, derived for the 920 consolidated loops, i.e., unique field lines. The properties, including the shear (Figure 7(a)), twist (Figures 7(b), (d)), and height (Figure 7(c)), of each unique model loop are plotted as open circles, with the color indicating the value from large (violet) to small (red). The area of each circle is proportional to the number of repeat observations (N from 1 to 31), and the vertical bar denotes the standard deviation of the measurements (see Section 3.3). Finally, the median values of each property, measured from the 920 unique field lines, over a 4 minute window are plotted as thick lines, with corresponding dashed curves showing the quartiles over the window.[2]

The conventional characterization of shear angle, $\theta_{\rm lp}$, measures the angle of the observed loop with respect to the PIL of

[2] The median values of the measurements from all 2728 loops are not significantly different and are, therefore, not displayed here.

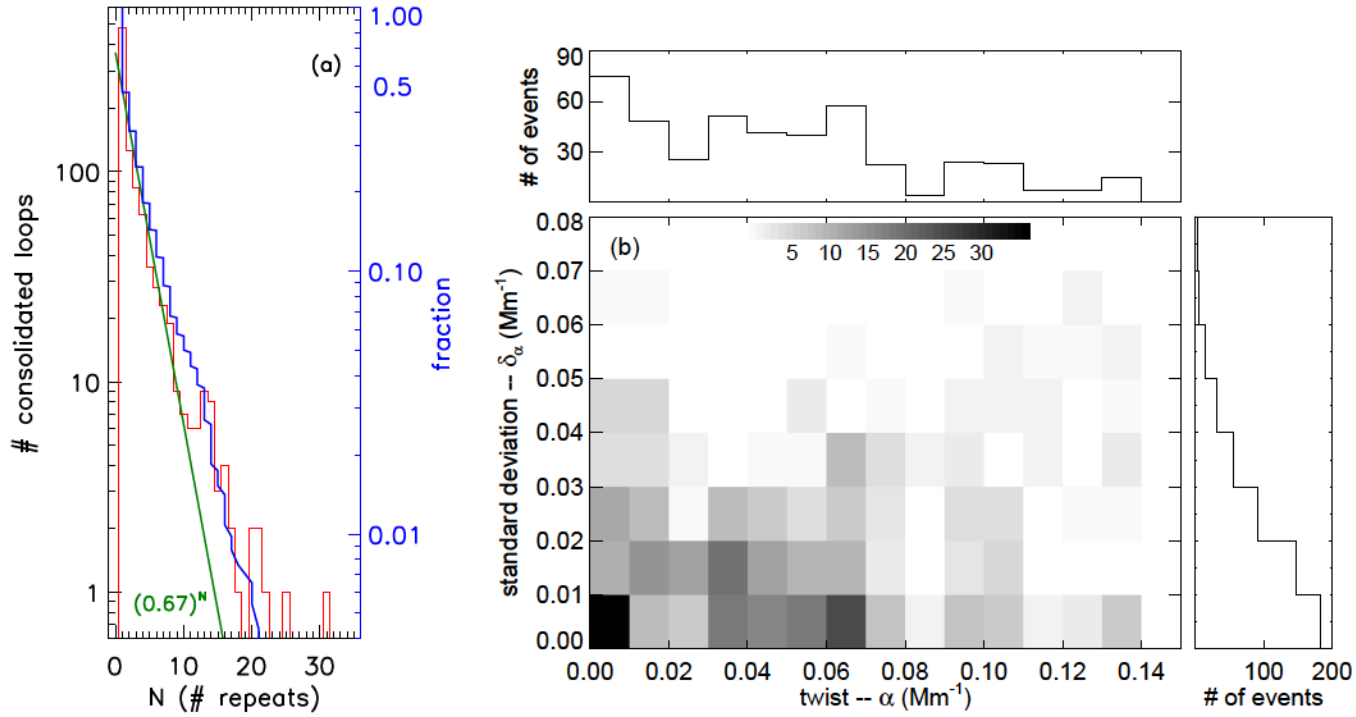

Figure 5. (a) Histograms of repeat measurements. The red curve is the histogram of N, read from the left axis, with the green curve showing an exponential fit. The blue curve, read from the right axis, is a cumulative histogram. (b) Histograms of the twist and its standard deviation of the 439 loops that are observed for more than once ($N > 1$).

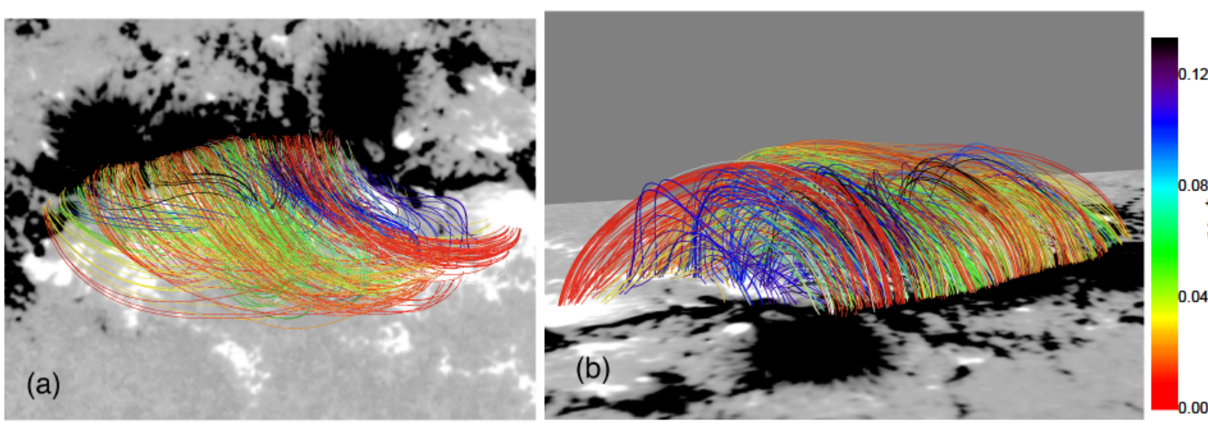

Figure 6. Top (a) and side (b) view of the model field lines of the unique reference loops. Colors indicate their values illustrated in the color bar.

the photospheric radial field. Figure 7(a) shows this value, but using the best-fit model field line projected onto the image plane. The 2D shear angle is measured from the normal vector $\hat{\boldsymbol{n}}$ of the local PIL, pointing from positive to negative polarities, to the local field line vector $\hat{f}$ also pointing from positive to negative polarity. Positive angles show the measurement from $\hat{\boldsymbol{n}}$ to $\hat{f}$ counterclockwise, and negative angles show the measurement clockwise. We note that $\theta_{\rm lp}$ is measured with respect to the PIL of the photospheric magnetogram, which often has a complex shape rather than a straight line. The curvature of the PIL introduces ambiguities in $\theta_{\rm lp}$ measurements, leading to, for example, some of the very large shear angle $|\theta_{\rm lp}|$ 90° in Figure 7(a). Despite the scattering due to the measurement ambiguity, overall, the shear angle $\theta_{\rm lp}$ is dominantly positive, reflecting a globally right-handed shear. Furthermore, it exhibits a decrease over time that is consistent with the strong-to-weak shear evolution reported by J. Qiu et al. (2023). In the present case, the median $\theta_{\rm lp}$ (black curve) decreases from more than 40° to about 20° over 50 minutes.

The shear angle $\theta_{\rm lp}^{p}$ of *potential field lines* traced from flare ribbons have been measured in the previous study (J. Qiu et al. 2023). In a realistic configuration, the shear angle of the potential field is not zero, and may fluctuate by 10°–20° (also see J. Qiu et al. 2017). The upshot is that the observed strong-to-weak shear evolution of PRFLs *does not* necessarily indicate an approach to a potential field, or relaxation.

The ORCCA fitting technique provides a more physically grounded measurement of magnetic shear in the form of the twist parameter . This quantity explicitly measures the field's departure from a potential field, since $= 0$ is potential. The evolution of , shown in both Figures 7(b) and (d), exhibits strong-to-weak evolution as decreases over 50 minutes from 0.12 to about 0.02 $\rm Mm^{-1}$. This makes a

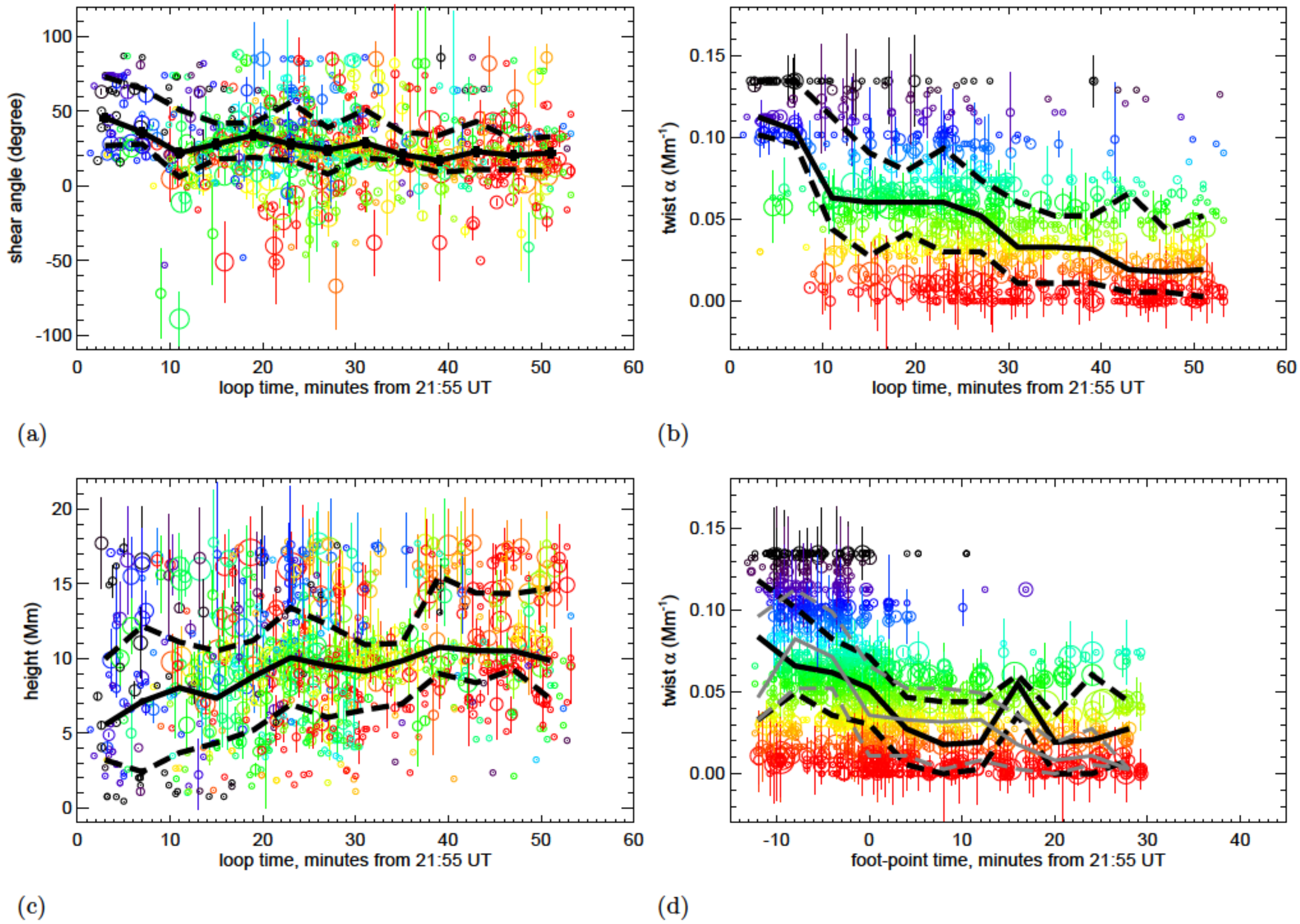

Figure 7. Properties of PRFLs, including the shear angle with the PIL (a), twist parameter (b), and height z_{max} (c) of unique model loops against the time when loops are observed. In each panel, the data points are plotted in color circles, with the color indicating the twist value, given in the color bar in Figure 6. The area of the circle is proportional to the number of repeat observations for each unique loop, and the vertical bar of the same color indicates one-half of the standard deviation of the measurements of the repeat loops. The thick solid black line shows the median value within a 4 minute window, and the thick dashed black lines show the quartiles of the values in the window. (d) Twist parameter against the time of the footpoint brightening (see Section 2 for definition) in both positive and negative magnetic fields. The median and quartiles of values within every 4 minutes are plotted in thick black/gray lines for the positive/negative footpoint timing.

compelling case that later-formed PRFLs are closer to a potential configuration. Moreover, it suggests a physical explanation for the strong-to-weak evolution in this two-ribbon flare: earlier formed loops have a larger twist, or a larger current per unit magnetic flux, than later-formed loops. This is the first time that the physical nature of the long-observed strong-to-weak shear evolution has been explained using observation-constrained 3D model.

It is notable that the traditional shear angle, θ_{lp}, turns out to correlate, to some extent, with . The Spearman correlation between θ_{lp} and is $\rho = 0.48$, among the consolidated loops. While this is not strong, it has virtually no probability of arising by chance. Thus, the empirical measure of shear, though with measurement ambiguities, is found to have some relation to the actual shear of the post-reconnection magnetic field.

Flare loops are observed in EUV passbands after they have been filled and heated by chromospheric evaporation and then cooled down to a few million kelvin to be visible in these images. This process leads to a significant time lag between the observed signatures of reconnection and heating, i.e., the footpoint brightening, and loop's appearance in EUV. The delay makes it very difficult to identify the feet of PRFLs. Now in possession of a 3D model of the PRFLs, we can track each loop to its conjugate feet in the lower atmosphere, and identify the time of its formation by reconnection.

Using our 3D field lines, we associate each coronal loop observed in a particular EUV band with the chromospheric footpoints that brighten in AIA 1600 Å to form the flare ribbon. The difference between the time of footpoint brightening and loop appearance defines a time delay Δt. Indeed, since each EUV loop is paired with both a positive and a negative footpoint, we measure two delays, Δt_+ and Δt_-, which should theoretically be the same. Figure 8 shows the distribution of these two measurements for each of the 920 reference loops, 570 fit from 304 Å (red) and 350 fit from 171 Å (blue). The scatter plot shows that the two delays, Δt_+ and Δt_-, are strongly correlated (Spearman $\rho = 0.56$), though they do not agree precisely. Most delays differ by less than 7 minutes (see dashed diagonals), which we take as the measurement uncertainty. Furthermore, we see that both wavelengths exhibit very similar distributions, with delays of roughly 24 minutes between reconnection (i.e., footpoint brightening) and loop appearance in the EUV passbands characterizing plasma temperature 1 MK. The implications of these results will be further discussed in Section 5.3.

Figure 7(d) plots the twist of consolidated loops versus the brightening time of their associated footpoint, in the same

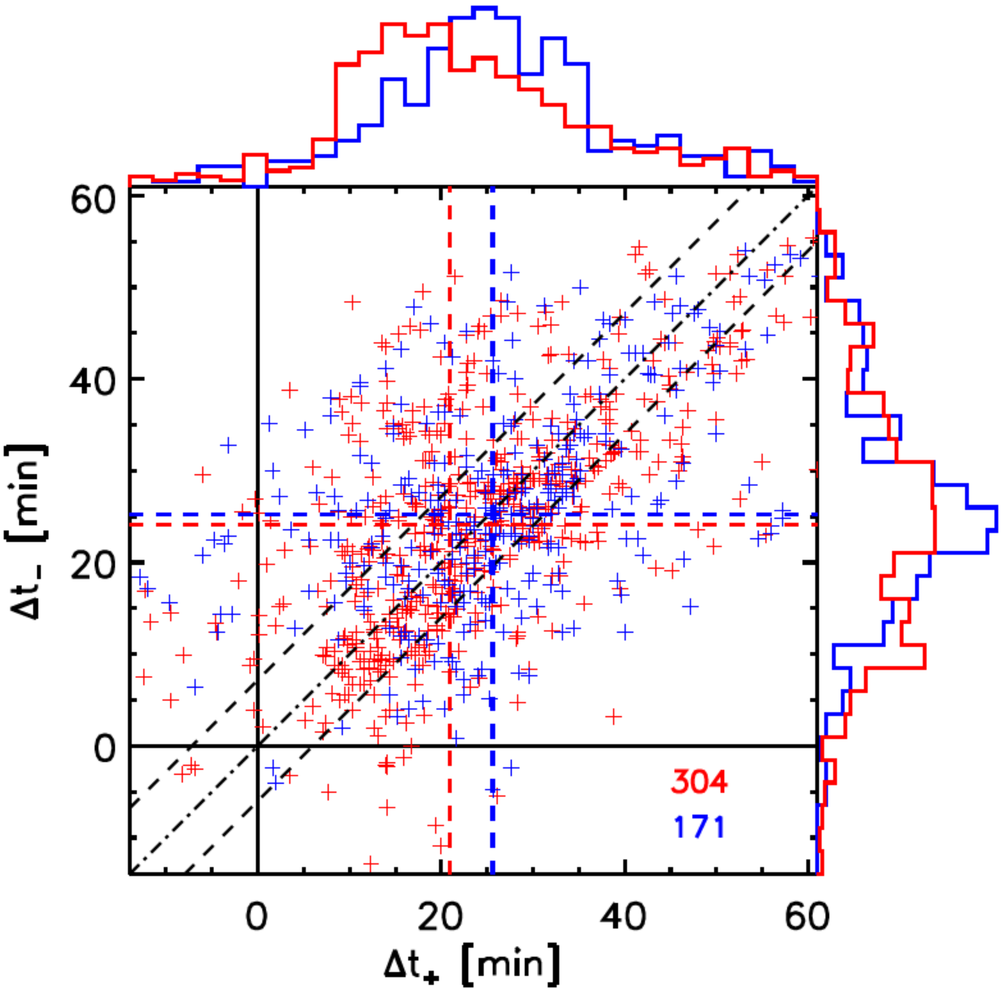

Figure 8. Plot of time delays Δt_+ and Δt_-. The central scatter plot shows Δt_- and Δt_+ for each reference loop as a cross: red for 304 Å, and blue for 171 Å. Vertical and horizontal dashed lines of matching color show the medians. A broken black line indicates $\Delta t_+ = \Delta t_-$, and dashed diagonals above and below it mark off the central quartiles of the distribution. Normalized histograms of each delay are plotted along the side and top in matching color for each wavelength.

format as Figure 7(b). Since each loop has two footpoints, it is represented by two circles on the plot. This also leads to two windowed-median curves, black and gray. Comparison between the figures shows that strong-to-weak evolution appears better organized by time of reconnection (d) than by time of loop appearance (b). The time axis is also displaced leftward on (d), beginning at negative time, due to the time delay.

The 3D model also reveals the outward ribbon motion coincides with decreasing in PRFL twist. Figure 9 displays values of at the feet of the full 3D loops over a magnetogram (grayscale). The spatial distribution exhibits a rather organized pattern with larger (violet to blue) lined along the inner edges of the ribbons close to the PIL. As the feet "move" away from the PIL, and from each other, becomes smaller (green to red). The spatial distribution of inside flare ribbons follows a pattern similar to that of flare ribbons spreading out over time (Figure 1(f)), further supporting that later-formed loops are taller with a larger footpoint separation, and are closer to the potential field.

In the standard picture of flare evolution, i.e., the CSHKP model, ongoing reconnection produces loops of increasing height. The association of 3D properties with flare loops provided by ORCCA allows us to quantitatively corroborate this picture, as in Figure 7(c), showing the maximum height z_{max} measured from the surface. The height of the loops increases over time, consistent with the standard picture. This also matches off-limb observations of flare arcades that grow in height (e.g., S. Masuda et al. 1994; T. G. Forbes & L. W. Acton 1996; D. Longcope et al. 2018).

In summary, we have used our new ORCCA fitting technique to show that the magnetic field following a flare is not potential, nor is it linear force free. Instead, the magnetic field is best described by a quasi-nonlinear force-free field with earlier formed loops having a larger force-free factor than later-formed loops. This also provides, for the first time, a physical explanation for the strong-to-weak shear evolution in this two-ribbon flare.

5. Discussions and Conclusions

5.1. Summary of Findings

The strong-to-weak shear evolution of PRFLs has been reported in observations for two decades. Without reliable 3D models of post-reconnection magnetic field, the physical nature of the observed strong-to-weak shear evolution has not been clear.

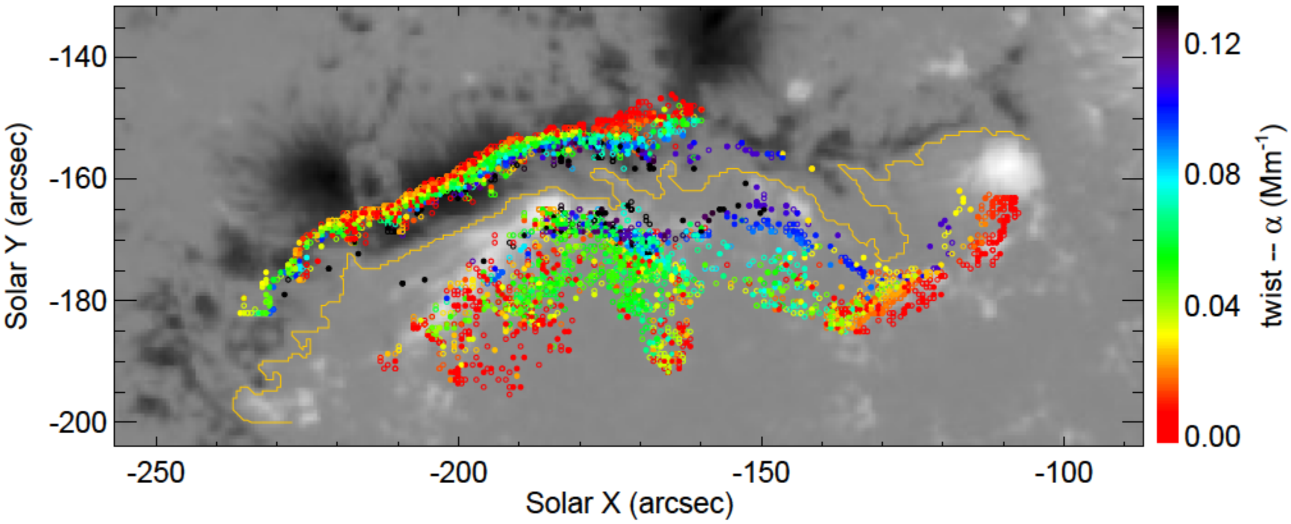

Figure 9. Distribution of at $z = 0$ for all best-fit model loops (open circle) and for the consolidated loops (filled circle), superimposed on a magnetogram of the radial component of the photospheric magnetic field in helioprojective coordinates (AIA image plane). The orange curve outlines the PIL of the radial magnetic field.

In this study, we have developed a novel method to construct 3D magnetic field of PRFLs. A large number of PRFLs identified in EUV images are fitted by magnetic field lines, with the constraint that these field lines must be anchored in flare ribbons observed in UV images. This ORCCA fitting method is successfully applied to an eruptive two-ribbon flare that exhibits strong-to-weak shear evolution.

With the 3D model, we find that PRFLs formed earlier have larger twist than later-formed PRLFs. During the flare evolution, as the two ribbons outlining the conjugate feet of the PRFLs expand away from the PIL and from each other, the PRFLs are taller, and their twist decreases. This study therefore provides, for the first time, a physical explanation of the long-observed strong-to-weak shear evolution using the observation-constrained model.

With the ORCCA capability to trace field lines of PRFLs to their feet in the chromosphere, we also find the time delay between footpoint brightening and appearance of PRFLs in the EUV passbands. In this flare, the median time delay of hundreds of PRFLs emitting at 1 MK is about 20 minutes. This is consistent with previous measurements of cooling delays, but our use of ORCCA fitting provides the first case where the delay is measured for individual loops in a flare.

These results, and the ORCCA technique enabling these findings, have important implications on post-reconnection magnetic modeling and along-the-loop hydrodynamic modeling. The progress in these modeling efforts will improve our understanding of flare energetics.

5.2. Implications on Post-reconnection Magnetic Modeling

Prior to this study, vector magnetograms have been analyzed to derive parameters characterizing the shear or twist in an active region. M. D. Kazachenko et al. (2022) analyzed vector magnetograms of the active region hosting the flare in this study, and found strong vertical electric currents I_z and shear $\mathcal{S}_{\rm ph}$ adjacent to the PIL separating the two flare ribbons. Note that shear is defined by M. D. Kazachenko et al. (2022) as

$$\mathcal{S}_{\rm ph} \equiv |B| \cos^{-1}\left(\frac{\boldsymbol{B}\cdot\boldsymbol{B}^p}{BB^p}\right)(\text{G degree}), \tag{2}$$

a parameter measuring the difference between the local vector magnetic field $\boldsymbol{B}$ and the potential field $\boldsymbol{B}^p$ extrapolated from the same vertical component B_z. The analysis was conducted using magnetograms at 21:41 UT, on the eve of the flare occurrence.

To place the of PRFLs from our study in the context of the active region evolution, we derive the vertical electric current and force-free parameter $_{\rm ph}$ from vector magnetograms of the photosphere, from 3 hr before the flare to 3 hr after the flare. During this period, the variation of the vertical magnetic field or flux is negligible (by 3% within the active region, and 6% within flare ribbons). The vertical currents and $_{\rm ph}$, on the other hand, exhibit nonnegligible changes after the flare. Figure 10 shows the distribution of the vertical electric current j_z and the force-free parameter ⟨ $_{\rm ph}$ before and after the flare. Here, the computation of ⟨ $_{\rm ph}$ is weighted by the vertical magnetic field B_z and averaged within 3 x 3 pixels to minimize large errors associated with weak B_z,

$$\langle\alpha_{\rm ph}\rangle = \frac{\int(\nabla\times\boldsymbol{B})_z B_z ds}{\int B_z^2 ds}. \tag{3}$$

It is shown that strong vertical currents and large twist are distributed along the PIL. After the flare, the total currents have grown from 2.6 to 3.2 $\times$ 10^{12} A in the positive ribbon, and from -3.4 to -3.9 $\times$ 10^{12} A in the negative ribbon. Nevertheless, the peak current density has decreased after the flare, and currents appear to spread away from the PIL, and become more diffused into the ribbons. A similar pattern has been observed in the ⟨ $_{\rm ph}$ distribution, with ⟨ $_{\rm ph}$ becoming smaller yet more diffused inside the flare ribbons after the flare. The evolution of the active region twist or currents reflect re-organization of magnetic fields by flare reconnection. On the other hand, the ⟨ $_{\rm ph}$ values are much larger than the PRFL- determined with the ORCCA method. The discrepancy may be physical: ⟨ $_{\rm ph}$ characterizes nonpotentiality in the photosphere, whereas PRFL- describes the magnetic field in the corona.

Y. Liu et al. (2023) recently examined the evolution of 21 active regions producing X-class flares (i.e., not including the active region in this study). They measured ⟨ $_{\rm ph}$ in a flare-

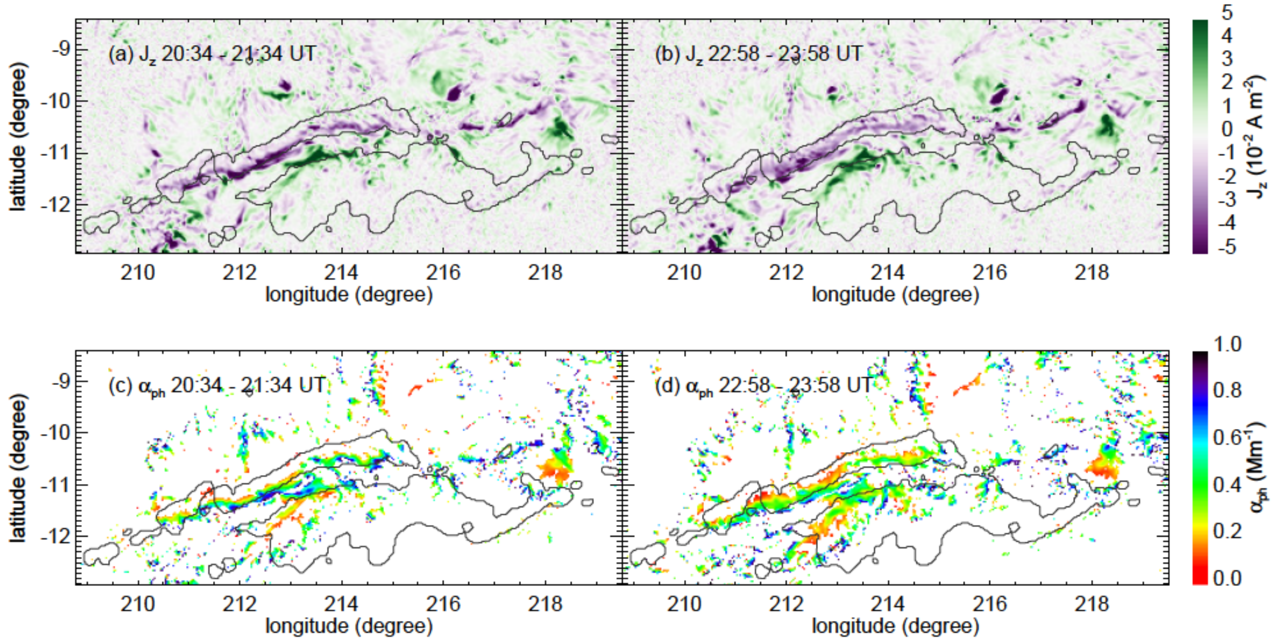

Figure 10. Top panels: distribution of vertical electric currents averaged for 72 minutes before (a) and after (b) the flare, respectively. Bottom panels: distribution of ⟨ averaged for 72 minutes before (c) and after (d) the flare. The black contours denote the flare ribbons, the same as in Figure 1(f). The maps are casted in CEA coordinates of heliographic longitudes and latitudes.

mask determined from Q-maps, and reported that, after the flare, ⟨ ph appears to be more smoothly distributed within the flare-mask, similar to the finding in this study. However, Y. Liu et al. (2023) studied different active regions, determined the flare-mask with a method different from ours, and computed ⟨ ph with a smoothing box of different size; therefore, the ⟨ ph values presented in Y. Liu et al. (2023) should not be directly compared with the values in this paper.

In summary, in this flare, the PRFL arcade is anchored in a region with strong electric currents and twist as measured in the vector magnetograms. The comparison suggests that, qualitatively, the PRFL distribution reflects the shear distribution originally built in the pre-reconnection field, perhaps in the form of a sheared-arcade (N. C. Joshi et al. 2017; J. T. Dahlin et al. 2022; A. Prasad et al. 2023). Measured by either ph or PRFL- , flare reconnection does not completely relax the field to an LFFF (S. K. Antiochos et al. 2002; D. Nandy et al. 2003; D. W. Longcope & A. Malanushenko 2008; X. Sun et al. 2012; Y. Liu et al. 2023). The ORCCA method developed in this study takes advantage of observations in the corona, chromosphere, and photosphere, and models the coronal magnetic field with the *connectivity* established from observations of flare ribbons and loops. Therefore, the distribution derived with this method provides crucial information that can lead to improved post-reconnection magnetic models and, henceforth, a better estimate of magnetic energy released in flares. This will be pursued in our future work.

5.3. Implications on Hydrodynamic Modeling

A significant amount of free magnetic energy released by flare reconnection is used to heat flare plasmas, producing prominent X-ray and EUV emissions in PRFLs and brightening at their feet. To date, we do not fully understand how plasmas in flare loops are heated to more than 10 MK and then cool down to 1 MK. One-dimensional along-the-field hydrodynamic simulations have been used to model this process (e.g., H. P. Warren 2006; D. W. Longcope 2014; J. C. Allred et al. 2015; A. F. Kowalski et al. 2017; G. S. Kerr et al. 2020; J. W. Reep et al. 2020). In solar flares, heating and cooling of the chromosphere and corona have to be studied coherently. Therefore, observational signatures from the chromosphere (flare ribbons) to the corona (PRFLs) along the *same* loop will provide crucial tests on these models. However, it has been challenging to identify the *same* loop from its conjugate feet in the chromosphere to the corona. The ORCCA method makes significant progress toward overcoming this long-standing obstacle. It traces an entire flare loop from the chromosphere to the corona, along which the tempo-spatial evolution of plasma emission in multiple wavelengths can be measured to provide an observational test on hydrodynamic models. As an example, Figure 8 shows the time delay of EUV emission in PRFLs with respect to their footpoint brightening, suggesting that the cooling time from reconnection to plasma emission at temperature 1 MK ranges between 10 and 30 minutes. Employing observations of PRFLs in multiple EUV wavelengths, it is possible to derive time delays of plasma emissions characterizing temperatures from 10–1 MK with respect to the UV brightening (and other dynamic signatures from spectroscopic observations) at their footpoints. This helps establish the time sequence of heating and cooling for individual PRFLs, which will be pursued in our future work.

Acknowledgments

We thank the referee for providing insightful comments and suggestions that helped improve the paper. This work was supported by NASA grant No. 80NSSC23K0414 and NSF grant No. AST-2407849. SDO is a mission of NASA's Living With a Star Program.

ORCID iDs

Jiong Qiu https://orcid.org/0000-0002-2797-744X

References

Allred, J. C., Kowalski, A. F., & Carlsson, M. 2015, ApJ, 809, 104
Antiochos, S. K., Karpen, J. T., & DeVore, C. R. 2002, ApJ, 575, 578
Antonucci, E., Gabriel, A. H., Acton, L. W., et al. 1982, SoPh, 78, 107
Asai, A., Yokoyama, T., Shimojo, M., et al. 2004, ApJ, 611, 557
Aschwanden, M. J. 2010, SoPh, 262, 399
Aschwanden, M. J., & Alexander, D. 2001, SoPh, 204, 91
Aschwanden, M. J., & Peter, H. 2017, ApJ, 840, 4
Aulanier, G., Janvier, M., & Schmieder, B. 2012, A&A, 543, A110
Bobra, M. G., & Couvidat, S. 2015, ApJ, 798, 135
Bobra, M. G., Sun, X., Hoeksema, J. T., et al. 2014, SoPh, 289, 3549
Bogachev, S. A., Somov, B. V., Kosugi, T., & Sakao, T. 2005, ApJ, 630, 561
Carmichael, H. 1964, NASSP, 50, 451
Dahlin, J. T., Antiochos, S. K., Qiu, J., & DeVore, C. R. 2022, ApJ, 932, 94
Fisher, G. H. 1987, ApJ, 317, 502
Fletcher, L., & Hudson, H. 2001, SoPh, 204, 69
Forbes, T. G., & Acton, L. W. 1996, ApJ, 459, 330
Grigis, P. C., & Benz, A. O. 2005, ApJL, 625, L143
Hinterreiter, J., Veronig, A. M., Thalmann, J. K., Tschernitz, J., & Pötzi, W. 2018, SoPh, 293, 38
Hirayama, T. 1974, SoPh, 34, 323
Inglis, A. R., & Gilbert, H. R. 2013, ApJ, 777, 30
Isobe, H., Shibata, K., & Machida, S. 2002, GeoRL, 29, 2014
Janvier, M., Aulanier, G., Pariat, E., & Démoulin, P. 2013, A&A, 555, A77
Ji, H., Huang, G., Wang, H., et al. 2006, ApJL, 636, L173
Joshi, N. C., Sterling, A. C., Moore, R. L., Magara, T., & Moon, Y.-J. 2017, ApJ, 845, 26
Kazachenko, M. D., Lynch, B. J., Savcheva, A., Sun, X., & Welsch, B. T. 2022, ApJ, 926, 56
Kazachenko, M. D., Lynch, B. J., Welsch, B. T., & Sun, X. 2017, ApJ, 845, 49
Kerr, G. S., Allred, J. C., & Polito, V. 2020, ApJ, 900, 18
Kitahara, T., & Kurokawa, H. 1990, SoPh, 125, 321
Kopp, R. A., & Pneuman, G. W. 1976, SoPh, 50, 85
Kowalski, A. F., Allred, J. C., Daw, A., Cauzzi, G., & Carlsson, M. 2017, ApJ, 836, 12
Lemen, J. R., Title, A. M., Akin, D. J., et al. 2012, SoPh, 275, 17
Li, T., Liu, L., Hou, Y., & Zhang, J. 2019, ApJ, 881, 151
Liu, C., & Wang, H. 2009, ApJL, 696, L27
Liu, W., Petrosian, V., Dennis, B. R., & Holman, G. D. 2009, ApJ, 693, 847
Liu, Y., Welsch, B. T., Valori, G., et al. 2023, ApJ, 942, 27
Longcope, D., Unverferth, J., Klein, C., McCarthy, M., & Priest, E. 2018, ApJ, 868, 148
Longcope, D. W. 2014, ApJ, 795, 10
Longcope, D. W., & Malanushenko, A. 2008, ApJ, 674, 1130
Malanushenko, A., Longcope, D. W., & McKenzie, D. E. 2009, ApJ, 707, 1044
Masuda, S., Kosugi, T., Hara, H., Tsuneta, S., & Ogawara, Y. 1994, Natur, 371, 495
Nandy, D., Hahn, M., Canfield, R. C., & Longcope, D. W. 2003, ApJL, 597, L73
Patsourakos, S., Vourlidas, A., Török, T., et al. 2020, SSRv, 216, 131
Pesnell, W. D., Thompson, B. J., & Chamberlin, P. C. 2012, SoPh, 275, 3
Prasad, A., Kumar, S., Sterling, A. C., et al. 2023, A&A, 677, A43
Qiu, J. 2009, ApJ, 692, 1110
Qiu, J., Alaoui, M., Antiochos, S. K., et al. 2023, ApJ, 955, 34
Qiu, J., & Cheng, J. 2022, SoPh, 297, 80
Qiu, J., & Fleming, R. 2025, SoPh, 300, 137
Qiu, J., Lee, J., Gary, D. E., & Wang, H. 2002, ApJ, 565, 1335
Qiu, J., Liu, W., Hill, N., & Kazachenko, M. 2010, ApJ, 725, 319
Qiu, J., & Longcope, D. W. 2016, ApJ, 820, 14
Qiu, J., Longcope, D. W., Cassak, P. A., & Priest, E. R. 2017, ApJ, 838, 17
Reep, J. W., Warren, H. P., Moore, C. S., Suarez, C., & Hayes, L. A. 2020, ApJ, 895, 30
Sakao, T. 1994, PhD thesis, Univ. Tokyo
Schou, J., Scherrer, P. H., Bush, R. I., et al. 2012, SoPh, 275, 229
Schrijver, C. J., DeRosa, M. L., Metcalf, T., et al. 2008, ApJ, 675, 1637
Sturrock, P. A. 1966, Natur, 211, 695
Su, Y., Golub, L., & Van Ballegooijen, A. A. 2007, ApJ, 655, 606
Su, Y. N., Golub, L., van Ballegooijen, A. A., & Gros, M. 2006, SoPh, 236, 325
Sun, X., Hoeksema, J. T., Liu, Y., et al. 2012, ApJ, 748, 77
Svestka, Z. 1980, RSPTA, 297, 575
Temmer, M., Veronig, A. M., Vršnak, B., & Miklenic, C. 2007, ApJ, 654, 665
Warren, H. P. 2006, ApJ, 637, 522
Warren, H. P., Crump, N. A., Ugarte-Urra, I., et al. 2018, ApJ, 860, 46
Wiegelmann, T., & Sakurai, T. 2021, LRSP, 18, 1
Yang, Y.-H., Cheng, C. Z., Krucker, S., & Hsieh, M.-S. 2011, ApJ, 732, 15
Yang, Y.-H., Cheng, C. Z., Krucker, S., Lin, R. P., & Ip, W. H. 2009, ApJ, 693, 132
Zimovets, I. V., Sharykin, I. N., & Gan, W. Q. 2020, ApJ, 891, 138